

Article

Orientation Relationship of the Intergrowth $\text{Al}_{13}\text{Fe}_3$ and $\text{Al}_{13}\text{Fe}_4$ Intermetallics Determined by Single-Crystal X-ray Diffraction

Yibo Liu ¹, Changzeng Fan ^{1,2,*} , Zhefeng Xu ^{1,2}, Ruidong Fu ^{1,2}, Bin Wen ¹  and Lifeng Zhang ^{1,3}

¹ State Key Laboratory of Metastable Materials Science and Technology, Yanshan University, Qinhuangdao 066004, China; 202121020059@stumail.ysu.edu.cn (Y.L.); zfxu@ysu.edu.cn (Z.X.); rdfu@ysu.edu.cn (R.F.); wenbin@ysu.edu.cn (B.W.); zhanglifeng@ncut.edu.cn (L.Z.)

² Hebei Key Lab for Optimizing Metal Product Technology and Performance, Yanshan University, Qinhuangdao 066004, China

³ School of Mechanical and Materials Engineering, North China University of Technology, Beijing 100144, China

* Correspondence: chzfan@ysu.edu.cn

Abstract: In the Al-Fe binary system, the $\text{Al}_{13}\text{Fe}_3$ phase as well as the $\text{Al}_{13}\text{Fe}_4$ phase has similar icosahedral building blocks like those appearing in quasicrystals. Therefore, it is of vital importance to clarify the formation process of these two phases. Coexistence of the $\text{Al}_{13}\text{Fe}_3$ and $\text{Al}_{13}\text{Fe}_4$ phases was discovered from the educts obtained with a nominal atomic ratio of Al/Fe of 9:2 by high-pressure sintering for the first time. Firstly, single crystal X-ray diffraction (SXRD) combined with a scanning electron microscope (SEM) with energy dispersive X-ray spectroscopy (EDX) measurement capabilities were adopted to determine the detailed crystal structures of both phases, which were sharply refined with regard to $\text{Al}_{13}\text{Fe}_3$ and $\text{Al}_{13}\text{Fe}_4$. Secondly, the orientation relationship between $\text{Al}_{13}\text{Fe}_3$ and $\text{Al}_{13}\text{Fe}_4$ was directly deduced from the SXRD datasets and the coexistence structure model was consequently constructed. Finally, seven pairs of parallel atomic planes and their unique orientation relations were determined from the reconstructed reciprocal space precession images. In addition, the real space structure model of the intergrowth crystal along with one kind of interfacial atomic structure were constructed from the determined orientation relations between two phases.

Keywords: $\text{Al}_{13}\text{Fe}_3$; $\text{Al}_{13}\text{Fe}_4$; high-pressure sintering; single crystal; structural refinement; orientation relationship



Citation: Liu, Y.; Fan, C.; Xu, Z.; Fu, R.; Wen, B.; Zhang, L. Orientation Relationship of the Intergrowth $\text{Al}_{13}\text{Fe}_3$ and $\text{Al}_{13}\text{Fe}_4$ Intermetallics Determined by Single-Crystal X-ray Diffraction. *Metals* **2024**, *14*, 463. <https://doi.org/10.3390/met14040463>

Academic Editor: Angelo Fernando Padilha

Received: 3 March 2024

Revised: 28 March 2024

Accepted: 12 April 2024

Published: 15 April 2024



Copyright: © 2024 by the authors. Licensee MDPI, Basel, Switzerland. This article is an open access article distributed under the terms and conditions of the Creative Commons Attribution (CC BY) license (<https://creativecommons.org/licenses/by/4.0/>).

1. Introduction

Al and Fe are the two most abundant metallic elements in the earth's crust. Due to their extensive sources and low cost, they are the two most commonly used metals in industry. Compared with other aluminum alloys, Fe forms a variety of Al-Fe intermetallic compounds with Al, having relatively high strength and hardness and possessing a wide range of applications [1–5]. Al-Fe alloy can not only partially replace titanium alloy in the aerospace field [6–9] but also reduce the research and development costs in the automotive manufacturing process [10–13]. Many researchers have carried out numerous exploration and research studies on refining alloy microstructure and improving intermetallic compound content [14–21]. In addition, Al-Fe alloy has been widely studied due to its unique structure, of which the quasicrystals of Al-Fe binary system were studied as early as 1986 [22]. Many quasicrystal-related phases, including some approximate phases in the Al-Fe system, have been discovered, such as the cubic phase AlFe [23,24], cubic phase Al_8Fe_5 [25], orthorhombic phase Al_5Fe_2 [26], triclinic crystal system Al_2Fe [27], monoclinic crystal system $\text{Al}_{13}\text{Fe}_4$ [28], and trigonal crystal system $\text{Al}_{13}\text{Fe}_3$ [29].

As a typical quasicrystalline approximant phase, the crystal structure of $\text{Al}_{13}\text{Fe}_4$ has been studied extensively [28,30–34]. It has also been found that the $\text{Al}_{13}\text{Fe}_4$ phase is an important intermedium phase between icosahedral and decagon quasicrystallines [35]. Early X-ray diffraction patterns suggested that this compound has an orthorhombic lattice [36,37].

Careful structural analysis showed a twinning feature of crystals, which resulted in an orthorhombic pseudo-symmetry [38,39]. There have been various discussions about the crystal structure of $\text{Al}_{13}\text{Fe}_4$. For example, Griger et al. determined the crystal structure of $\text{Al}_{13}\text{Fe}_4$ by powder X-ray diffraction and concluded that the occupancy of the Al2 atom at the $2m$ Wykoff site is 0.7 [40]. Grin et al. [28] determined the crystal structure of $\text{Al}_{13}\text{Fe}_4$ by the single-crystal X-ray diffraction method. The difference lies in that the occupancy of the Al2 atom at the $2m$ Wykoff site is refined to 0.92. Subsequently, Popevic et al. [33] also performed single-crystal structure determinations and found that there was no vacancy defect in the crystal.

Moreover, the $\text{Al}_{13}\text{Fe}_3$ phase of the trigonal system is the quasicrystalline approximate phase of the Al-Fe binary system. It was firstly observed with transmission electron microscopy by Chandrasekaran et al. in 1988 [41] and was believed to be a new rhombohedral phase. Later, in 1992, Tsuchimo et al. [42] also found this phase when studying the iron-rich phase in the Al-Fe system. They believed that the space group of this phase belonged to $R3c$ or $R\bar{3}c$ but did not provide its exact crystal structure. In 2018, the fine crystal structure of this phase was determined by our group for the first time by the single-crystal X-ray diffraction method [29]. The cell parameters of this phase are refined to $a = b = 14.5784(9)$, $c = 7.5020(5)$, $\alpha = \beta = 90^\circ$, and $\gamma = 120^\circ$ with the $R3c$ space group.

Previous research works mainly focused on characterizing the existence of the $\text{Al}_{13}\text{Fe}_4$ phase as well as its thermodynamic and dynamical behaviors under different processing conditions [43–48]. There are also a number of works mentioning the co-existence of $\text{Al}_{13}\text{Fe}_4$ with a pure Al matrix or another phase like Al_5Fe_2 [49,50]. However, the orientation relationship between $\text{Al}_{13}\text{Fe}_4$ and Al_5Fe_2 has only very recently been reported by Chatelier et al. as far as we know using surface X-ray diffraction [51]. The orientation relationship between Al_2Fe and Al_5Fe_2 has been studied very recently by our group [52]. However, there are no related works on the orientation relationship between $\text{Al}_{13}\text{Fe}_3$ and $\text{Al}_{13}\text{Fe}_4$, to the best of our knowledge, possibly due to the $\text{Al}_{13}\text{Fe}_3$ phase not having been discovered until 2018 by our group [29]. Information on the orientation relationship between coexistence phases can reveal the growth process of crystals and the arrangement of atoms at the interface to a certain extent. Therefore, in the following, we will introduce the discovery of the coexistence of $\text{Al}_{13}\text{Fe}_3$ and $\text{Al}_{13}\text{Fe}_4$. Firstly, sample preparation by the high-pressure sintering method and the analysis of the SXRD datasets will be introduced. Secondly, the solving and refinement process of the crystal structures of these two phases as well as the acquisition of the orientation relationship of the two phases in the real space will be illustrated. The parallel atomic planes present between the coexisting phases were analyzed, and a preferential interface was constructed by referring to the reconstructed precession images in reciprocal space.

2. Materials and Methods

The high-purity elements aluminum (Al, Aladdin Industrial Corporation, Shanghai, China) and iron (Fe, Alfa Aesar, Tianjin, China) with indicated purities of 99.95% and 99.9%, respectively, were combined at a stoichiometric ratio of 9:2, weighing 2 g in total. The mixture was thoroughly ground in an agate mortar. The resulting powders were then placed in a cemented carbide grinding mold with a 5 mm diameter and compressed into a tablet at approximately 4 MPa pressure for a duration of 3 min. A cylindrical block was successfully formed without any deformations or cracks. Further information regarding the high-pressure sintering process conducted using a six-anvil, high-temperature, high-pressure apparatus can be found in a study by Liu and Fan (2018) [34]. The samples underwent pressurization up to 6 GPa, were heated to 1573 K for 10 min, were subsequently cooled to 1423 K, were maintained at that temperature for 30 min, and were finally rapidly cooled to room temperature by deactivating the furnace power. A fragment of a singular crystal measuring $0.10 \times 0.06 \times 0.06 \text{ mm}^3$ was chosen and affixed to a glass fiber for the purpose of conducting single-crystal X-ray diffraction analyses. The diffraction assessments were performed using a four-circle single-crystal X-ray diffractometer (Bruker D8 Venture,

Bruker AXS GmbH, Karlsruhe, Germany). To examine the morphology and chemical composition, a scanning electron microscope (SEM, Hitachi S-3400N model, Hitachi, Tokyo, Japan) equipped with energy dispersive X-ray spectroscopy (EDX) capabilities (EDAX Inc., Mahwah, NJ, USA) was employed, operating at a cathode voltage of 20 kV and a current of 80 mA (see Figure S1 and Table S1 in the Supplementary Materials).

The APEX3 program [53] was used to process all datasets from SXRD. Its capabilities include indexing, integration, scaling, absorption correction [54], space group determination, structural solving, and refinement [55,56]. The Diamond program (Version 4.6.8) [57] was utilized to draw the structural models, while the ToposPro package (Version 5.5.2.0) [58] was used to analyze the building clusters of the studied phases.

3. Results

3.1. Single-Crystal XRD Patterns

Figure 1 shows the diffraction points in the reciprocal space of the entire sample, which were obtained from 11 runs of SXRD measurements. As depicted in Figure 1a, these diffraction points can be distinctly categorized into three distinct datasets. The gray and yellow diffraction points represent the $\text{Al}_{13}\text{Fe}_3$ phase, the gray diffraction point corresponds to the $\text{Al}_{13}\text{Fe}_3$ -1 phase, and the yellow diffraction point corresponds to the $\text{Al}_{13}\text{Fe}_3$ -2 phase. The green diffraction points represent the $\text{Al}_{13}\text{Fe}_4$ phase. Figure 1b–d show the diffraction points projection of any two datasets so that it can be more clearly seen that they belong to different datasets. An individual analysis of the three datasets was conducted. The SXRD analysis of the sample involved a total of 11 runs, resulting in the collection of 9913 diffraction points in reciprocal space when the criterion of $I/\sigma(I)$ equaled 7 for phase indexing. Within these diffraction points, 4572 were attributed to the $\text{Al}_{13}\text{Fe}_3$ -1 phase, 1213 to the $\text{Al}_{13}\text{Fe}_3$ -2 phase, and 2342 to the $\text{Al}_{13}\text{Fe}_4$ phase. The remaining 1786 diffraction points were associated with anomalous phases, such as amorphous structures or very small crystalline phases that could not be indexed to determine a unit cell.

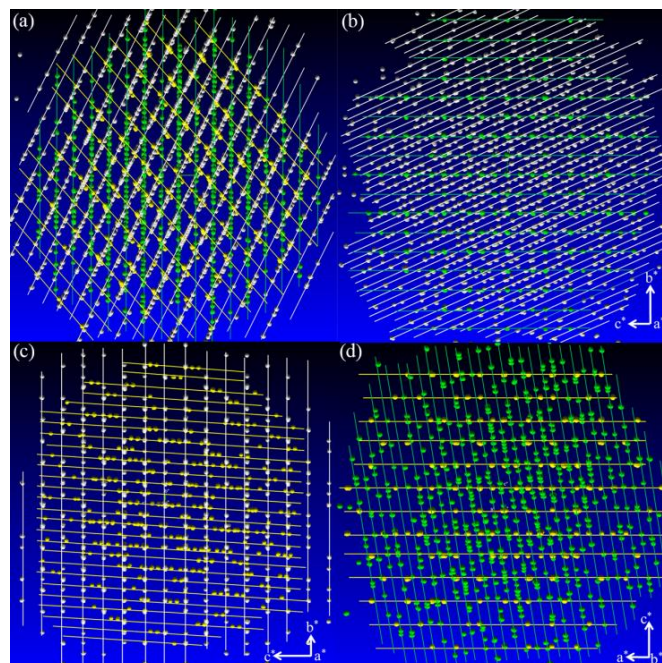


Figure 1. Diffraction spots of the entire sample in the reciprocal space. (a) Projection of three sets of data in reciprocal space in a random direction; (b) projection of the $\text{Al}_{13}\text{Fe}_3$ -1 phase and $\text{Al}_{13}\text{Fe}_4$ phase along the a^* axis of the $\text{Al}_{13}\text{Fe}_4$ phase; (c) projection of the $\text{Al}_{13}\text{Fe}_3$ -1 phase and $\text{Al}_{13}\text{Fe}_3$ -2 phase along the a^* axis of the $\text{Al}_{13}\text{Fe}_3$ -1 phase; (d) projection of the $\text{Al}_{13}\text{Fe}_3$ -2 phase and $\text{Al}_{13}\text{Fe}_4$ phase along the b^* axis of the $\text{Al}_{13}\text{Fe}_3$ -2 phase.

Figures 2–4 depict the reciprocal lattice patterns and crystal structure diagram of the $\text{Al}_{13}\text{Fe}_3$ and $\text{Al}_{13}\text{Fe}_4$ phases projected in different directions. The arrangement of diffraction points in reciprocal space appears orderly for each phase. The first dataset (highlighted in gray in Figure 1) corresponds to lattice parameters $a = b = 14.61 \text{ \AA}$, $c = 7.70 \text{ \AA}$, $\alpha = \beta = 90^\circ$, and $\gamma = 120^\circ$, consistent with those of the $\text{Al}_{13}\text{Fe}_3$ phase as depicted in Figure 2. The second dataset (highlighted in green in Figure 1) is characterized by lattice parameters $a = 15.51 \text{ \AA}$, $b = 8.09 \text{ \AA}$, $c = 12.50 \text{ \AA}$, $\alpha = \gamma = 90^\circ$, and $\beta = 107.76^\circ$, aligning with the properties of the $\text{Al}_{13}\text{Fe}_4$ phase as shown in Figure 3. The third dataset (highlighted in yellow in Figure 1) is identified as being identical to the first dataset.

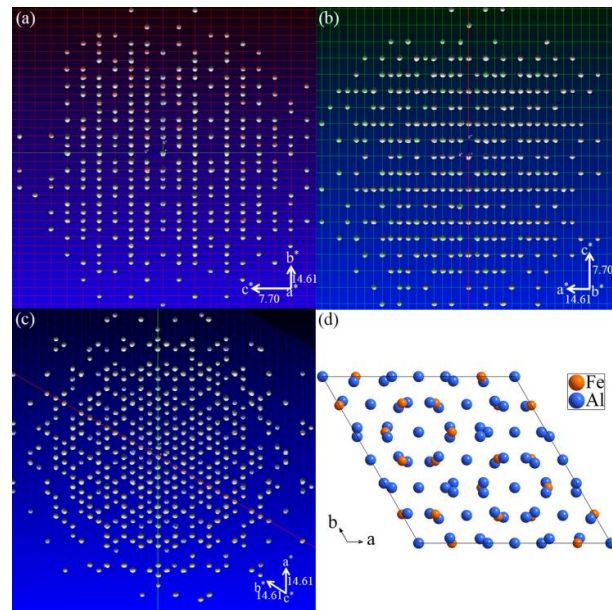


Figure 2. Reciprocal lattice patterns and crystal structure diagram of the $\text{Al}_{13}\text{Fe}_3$ -1 phase projected in different directions: (a) a^* axis; (b) b^* axis; (c) c^* axis; (d) c axis.

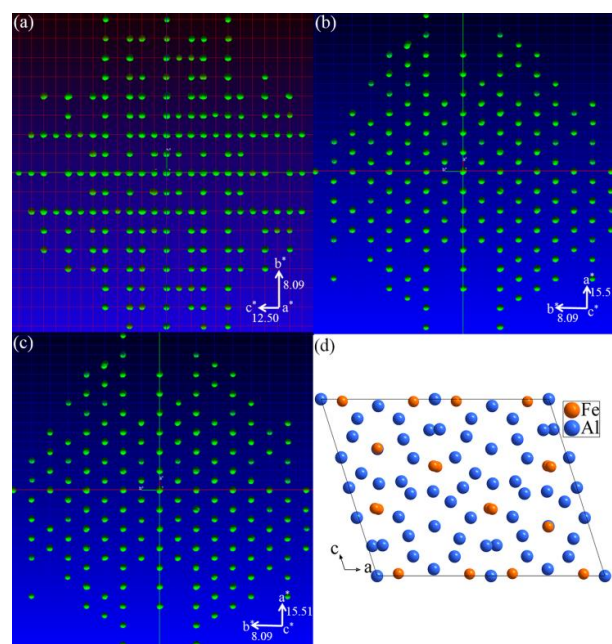


Figure 3. Reciprocal lattice patterns and crystal structure diagram of $\text{Al}_{13}\text{Fe}_4$ phase projected in different directions: (a) a^* axis; (b) b^* axis; (c) c^* axis; (d) b axis.

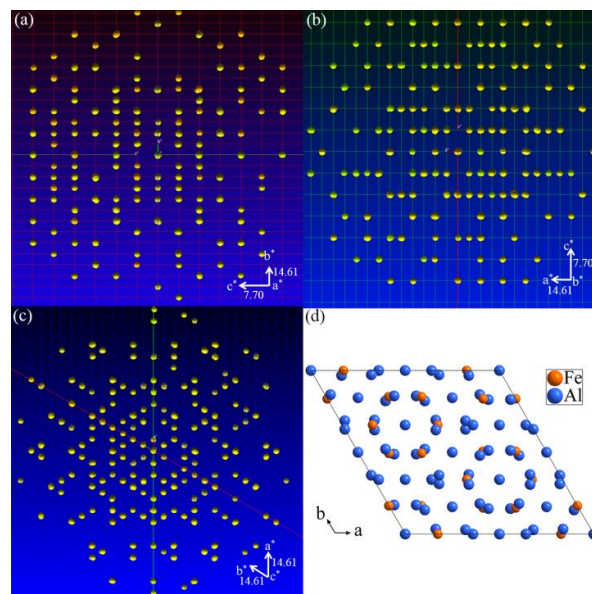


Figure 4. Reciprocal lattice patterns and crystal structure diagram of the $\text{Al}_{13}\text{Fe}_3$ -2 phase projected in different directions: (a) a^* axis; (b) b^* axis; (c) c^* axis; (d) c axis.

3.2. Crystal Structure Refinement of $\text{Al}_{13}\text{Fe}_3$ Phase and $\text{Al}_{13}\text{Fe}_4$ Phase

The crystallographic information, data collection, and structure refinement details for the $\text{Al}_{13}\text{Fe}_3$ and $\text{Al}_{13}\text{Fe}_4$ phases are outlined in Table 1. The crystallographic parameters of both phases conform to the standards set by international crystallography for the rationalization of crystal structures.

Table 1. Crystallographic and experimental data of $\text{Al}_{13}\text{Fe}_3$ and $\text{Al}_{13}\text{Fe}_4$.

Chemical Formula	$\text{Al}_{13}\text{Fe}_3$	$\text{Al}_{13}\text{Fe}_4$
$a, b, c / \text{\AA}$	14.5956(9), 14.5956(9), 7.6929(4)	15.498(4), 8.0814(17), 12.488(3)
$\alpha, \beta, \gamma / ^\circ$	90, 90, 120	90, 107.790(8), 90
$V / \text{\AA}^3$	1419.27(19)	1489.2(6)
Z	1	24
Space group	$R\bar{3}c$	$C2/m$
Crystal system	Trigonal	Monoclinic
Diffractometer	Bruker D8 Venture Photon 100 COMS	
Monochromator	Graphite	
$T_{\text{meas}} / \text{K}$	300(2)	
Radiation	Mo-K α , $\lambda = 0.71073$ (Å)	
Scan mode	φ and ω scan	
Time per step/s	6	
Absorption correction	Multi-scan	
F(000)	1482	1638
θ range/ $^\circ$	4.84~27.33	3.12~27.49
μ / mm^{-1}	5.69	6.82
No. measured reflections	19200	3922
No. unique reflections	367	1423
No. observed reflections ($I > 2\sigma(I)$)	341	756
No. reflections used in refinement	367	1423
No. parameters used in refinement	28	128
Reflection range	$-18 \leq h \leq 18, -18 \leq k \leq 18, -9 \leq l \leq 9$	$-18 \leq h \leq 11, -9 \leq k \leq 9, -16 \leq l \leq 13$
R_{int}	0.077	0.102
$R(\sigma)$	0.0152	0.178

Table 1. Cont.

Chemical Formula	Al ₁₃ Fe ₃	Al ₁₃ Fe ₄
Final <i>R</i> indices ($F_{\text{obs}} > 4\sigma(F_{\text{obs}})$)	$R_1 = 0.033, \omega R_2 = 0.0710$	$R_1 = 0.080, \omega R_2 = 0.223$
<i>R</i> indices (all data)	$R_1 = 0.034, \omega R_2 = 0.0710$	$R_1 = 0.169, \omega R_2 = 0.223$
Goodness of fit	1.326	1.07
The maximum residual electron densities	0.52 (1.43 Å from Al3)	1.71 (0.94 Å from Al14)
The minimum residual electron densities	−0.71 (0.72 Å from Al3)	−2.04 (0.89 Å from Al3)

Table 2 shows the equivalent isotropic displacement parameters (U_{eq}), fractional atomic coordinates, and atomic occupancy (Occ.) of the Al₁₃Fe₃ phase. It is noteworthy that all atoms in this structure are fully occupied. Comparing the current refined crystal structure model with the Al₁₃Fe₃ phase identified in 2018 [29] reveals some differences: we find that the Al3 atom is located at the 36*f* Wyckoff position in the present refined Al₁₃Fe₃ structure model rather than two 18*b* Wyckoff positions in the previous one, resulting in its space group changing from *R3c* to *R3̄c*.

Table 2. The equivalent isotropic displacement parameters (Å^2), fractional atomic coordinates, and atomic occupancy of the Al₁₃Fe₃ phase.

Label	Site	<i>x</i>	<i>y</i>	<i>z</i>	Occ.	U_{eq}
Fe1	18 <i>e</i>	0.333333	0.49355 (6)	0.416667	1	0.0061 (2)
Al1	18 <i>e</i>	0.35988 (13)	0.35988 (13)	0.250000	1	0.0110 (4)
Al2	6 <i>a</i>	0.333333	0.666667	0.416667	1	0.0180 (8)
Al3	36 <i>f</i>	0.48065 (11)	0.63616 (12)	0.24732 (18)	1	0.0188 (4)
Al4	18 <i>d</i>	0.166667	0.333333	0.333333	1	0.0183 (5)

The Al₁₃Fe₃ phase's building units were analyzed using the nanocluster method within the Topospro software (Version 5.5.2.0). The structural model of Al₁₃Fe₃ can be characterized by a single type of cluster, Al3(1)(1@12), which is an icosahedral cluster with the Al3 atom positioned at the cluster's center. In Figure 5a, the central atoms and the isolated atoms (atoms in the purple circle, which refers to the single atom that the structural model can contain to fill the space between the nanoclusters [59]) of the cluster were depicted within the Al₁₃Fe₃ unit cell. The cluster assembly model of the Al₁₃Fe₃ unit cell along the direction [001] is shown in Figure 5b. The clusters are connected in two ways: collinear and coplanar. In Figure 6, the surroundings of Al4 and Fe1 atoms are depicted. Al4 atoms are encircled by a total of 12 atoms: 4 Al1, 6 Al3, and 2 Fe1 atoms. On the other hand, Fe1 atoms are surrounded by nine atoms: two Al1, one Al2, four Al3, and two Al4 atoms. The closest distance between Fe1 and Al4 atoms measures 2.4715 Å.

Table 3 shows the equivalent isotropic displacement parameters (U_{eq}), fractional atomic coordinates, and atomic occupancy (Occ.) of the Al₁₃Fe₄ phase. All atoms in this structure are fully occupied which is nearly identical to the structure model of Sugiyama et al. reported in 2012 [60]. It should be noted that the 'EADP AL2 AL3 AL6' instruction was used to eliminate the N.P.D. alerts for Al2 and Al6 atoms and the ADP alert for the Al3 atom that are caused by these atoms during the refinement process of the Al₁₃Fe₄ phase (see the Al₁₃Fe₄ CIF file in the Supplementary Materials).

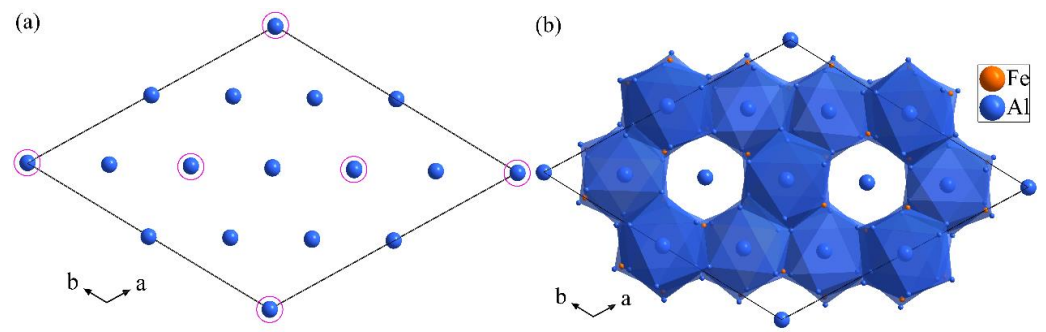


Figure 5. Cluster assembly of the $\text{Al}_{13}\text{Fe}_3$ phase in a unit cell: (a) the central atoms and isolated atoms of the cluster; (b) cluster assembly model.

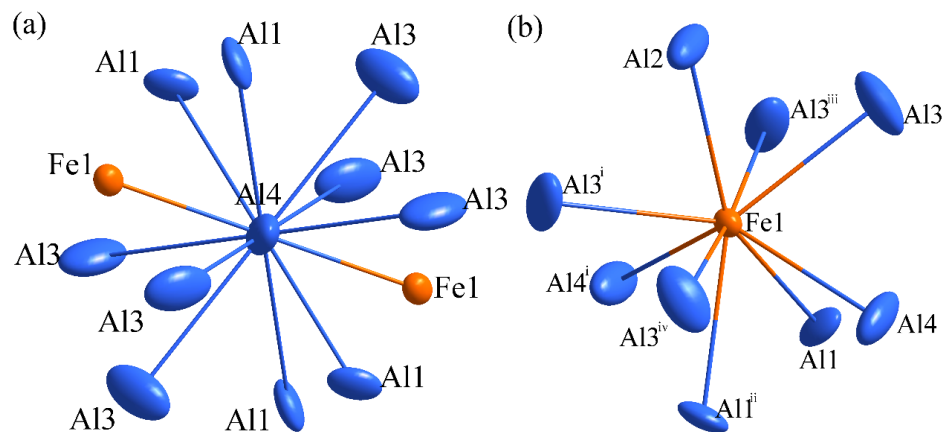


Figure 6. Atomic environment diagram: (a) Al4 atom; (b) Fe1 atom. Symmetry codes: (i) $-x + 2/3, -x + y + 1/3, -z + 5/6$; (ii) $-y + 2/3, x - y + 1/3, z + 1/3$; (iii) $y - 1/3, -x + y + 1/3, -z + 1/3$; (iv) $-y + 1, -x + 1, z + 1/2$.

Table 3. The equivalent isotropic displacement parameters (\AA^2), fractional atomic coordinates, and atomic occupancy of the $\text{Al}_{13}\text{Fe}_4$ phase.

Label	Site	x	y	z	Occ.	U_{eq}
Fe1	4i	0.0855 (3)	0.000000	0.3823 (3)	1	0.0043 (9)
Fe2	4i	0.4019 (3)	0.000000	0.6228 (3)	1	0.0065 (9)
Fe3	4i	0.0908 (3)	0.000000	0.9885 (3)	1	0.0056 (10)
Fe4	4i	0.4028 (3)	0.000000	0.9863 (3)	1	0.0046 (9)
Fe5	8j	0.32011(18)	0.2933 (3)	0.27793(18)	1	0.0068 (7)
Al1	4i	0.0670 (6)	0.000000	0.1738 (6)	1	0.0113 (18)
Al2	4i	0.3213 (6)	0.000000	0.2812 (6)	1	0.0112 (11)
Al3	4i	0.2381 (6)	0.000000	0.5339 (6)	1	0.0112 (11)
Al4	4i	0.0734 (6)	0.000000	0.5801 (6)	1	0.0111 (18)
Al5	4i	0.2415 (6)	0.000000	0.9614 (7)	1	0.0104 (17)
Al6	4i	0.4786 (6)	0.000000	0.8297 (6)	1	0.0112 (11)
Al7	2d	0.500000	0.000000	0.500000	1	0.011 (2)
Al8	4i	0.3060 (6)	0.000000	0.7729 (6)	1	0.0109 (17)
Al9	4i	0.0862 (6)	0.000000	0.7888 (6)	1	0.0098 (18)
Al10	8j	0.1859 (4)	0.2172 (7)	0.1112 (4)	1	0.0096 (14)
Al11	8j	0.3673 (4)	0.2116 (7)	0.1101 (4)	1	0.0103 (13)
Al12	8j	0.1772 (4)	0.2211 (7)	0.3343 (4)	1	0.0118 (13)
Al13	8j	0.4920 (4)	0.2328 (6)	0.3296 (4)	1	0.0082 (13)
Al14	8j	0.3636 (4)	0.2198 (7)	0.4781 (4)	1	0.0108 (13)
Al15	4g	0.000000	0.2495 (9)	0.000000	1	0.0086 (19)

We focused on the structural model of $\text{Al}_{13}\text{Fe}_4$. It was discovered that the structure of $\text{Al}_{13}\text{Fe}_4$ can be explained using two different cluster models: $\text{Al}_{15}(1)(1@12)$ and $\text{Al}_{17}(2)(1@12@46)$. The $\text{Al}_{15}(1)(1@12)$ cluster is an 18-hedron cluster with Al15 atom as the center, which can be seen in Figure 7c. The Al17 atom serves as the heart of the complicated double-shell cluster referred to as $\text{Al}_{17}(2)(1@12@46)$. Twelve coordinated atoms (Al12, Al13, Al14, and Fe2) make up the first shell, or inner shell, which is represented as an icosahedron in Figure 7a. The centered Al17 and Al12, Al13, Al14, and Fe2 have atomic distances of 3.242 Å, 2.816 Å, 2.711 Å, and 2.468 Å, respectively. The outer shell consists of atoms that are coordinated, with 46 atoms, including 4 Al1 atoms, 4 Al10 atoms, 4 Al11 atoms, 8 Al12 atoms, 6 Al3 atoms, 4 Al4 atoms, 2 Al6 atoms, 2 Al8 atoms, 4 Al9 atoms, 4 Fe1 atoms, and 4 Fe5 atoms as shown in Figure 7b. These two types of clusters are closely connected to form the global crystal structure of the $\text{Al}_{13}\text{Fe}_4$ phase as shown in Figure 7d. Figure 8 illustrates the surroundings of the Al17 and Al15 atoms. Each Al17 atom is encompassed by 12 neighboring atoms, comprising 3 Al13, four Al14, 2 Al12, and 2 Fe2 atoms and 1 Al1 atom. Similarly, each Al15 atom is surrounded by 12 neighboring atoms, which includes 2 Al1, 2 Al6, 2 Al10, 2 Al11, 2 Fe3, and 2 Fe4 atoms.

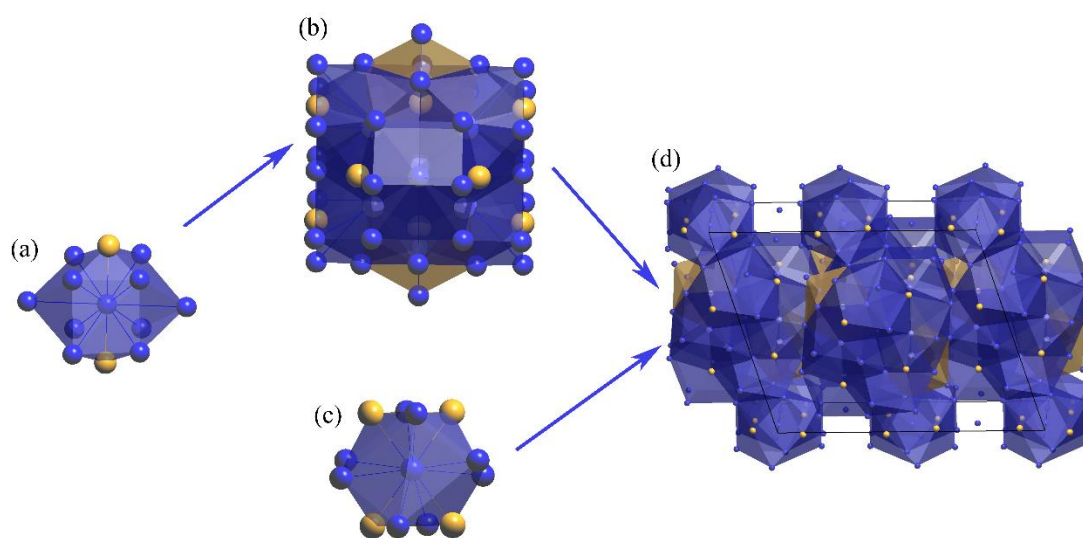


Figure 7. The cluster in the $\text{Al}_{13}\text{Fe}_4$ phase (The yellow atoms represent the Fe atoms and the blue atoms represent the Al atoms). (a) The inner shell of the $\text{Al}_{17}(2)(1@12@46)$ cluster; (b) the outer-shell of the $\text{Al}_{17}(2)(1@12@46)$ cluster; (c) the $\text{Al}_{15}(1)(1@12)$ cluster; (d) cluster assembly model in the $\text{Al}_{13}\text{Fe}_4$ unit cell.

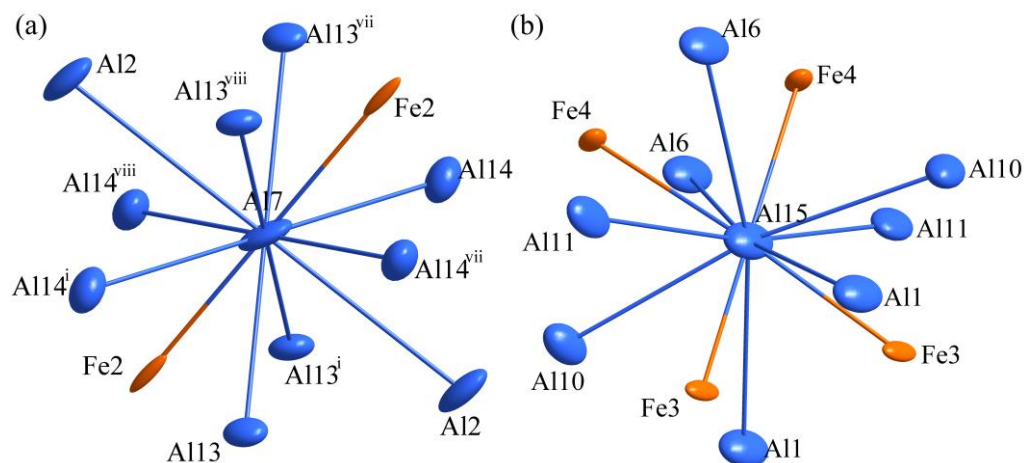


Figure 8. Atomic environment diagram: (a) Al17 atom; (b) Al15 atom. Symmetry codes: (i) $x, -y, z$; (vii) $-x + 1, y, -z + 1$; (viii) $-x + 1, -y, -z + 1$.

There are two interesting phenomena: First, all of the atoms in the $\text{Al}_{13}\text{Fe}_3$ and $\text{Al}_{13}\text{Fe}_4$ phases are completely occupied, and there are no disordered defects. Second, through topological analysis of the structures of $\text{Al}_{13}\text{Fe}_3$ and $\text{Al}_{13}\text{Fe}_4$, twisted icosahedrons were found in both of these structures as building units. We deduce that it is the structural similarity that governs the intergrowth between the two phases.

3.3. Structure Models of the $\text{Al}_{13}\text{Fe}_3$ and $\text{Al}_{13}\text{Fe}_4$ Intergrowth Phases in Real Space

The crystal structures of the $\text{Al}_{13}\text{Fe}_3$ and $\text{Al}_{13}\text{Fe}_4$ phases are provided in the section above. The orientation matrix of these two phases in reciprocal space was used to construct the real space orientation model, as described in this section. For the precise construction approach of the structural models for the intergrowth $\text{Al}_{13}\text{Fe}_3$ phase and $\text{Al}_{13}\text{Fe}_4$ phase in real space, please refer to Appendix A. First, the orientation matrix of three phases in reciprocal space was determined in APEX3 software (v2018.1–0). Next, utilizing the fundamental correspondence between reciprocal and real spaces, the orientation matrix of the three phases in real space was obtained, and finally, the orientation model of three-phase single-cell edges in real space was obtained. The cell edges of the $\text{Al}_{13}\text{Fe}_3$ -1, $\text{Al}_{13}\text{Fe}_3$ -2, and $\text{Al}_{13}\text{Fe}_4$ phases are depicted in Figure 9a as black, purple, and blue frames, respectively. Lastly, by adding atoms to the cell edges, the comprehensive orientated structural models of the $\text{Al}_{13}\text{Fe}_3$ -1, $\text{Al}_{13}\text{Fe}_3$ -2, and $\text{Al}_{13}\text{Fe}_4$ phases in real space were generated, as displayed in Figure 9b.

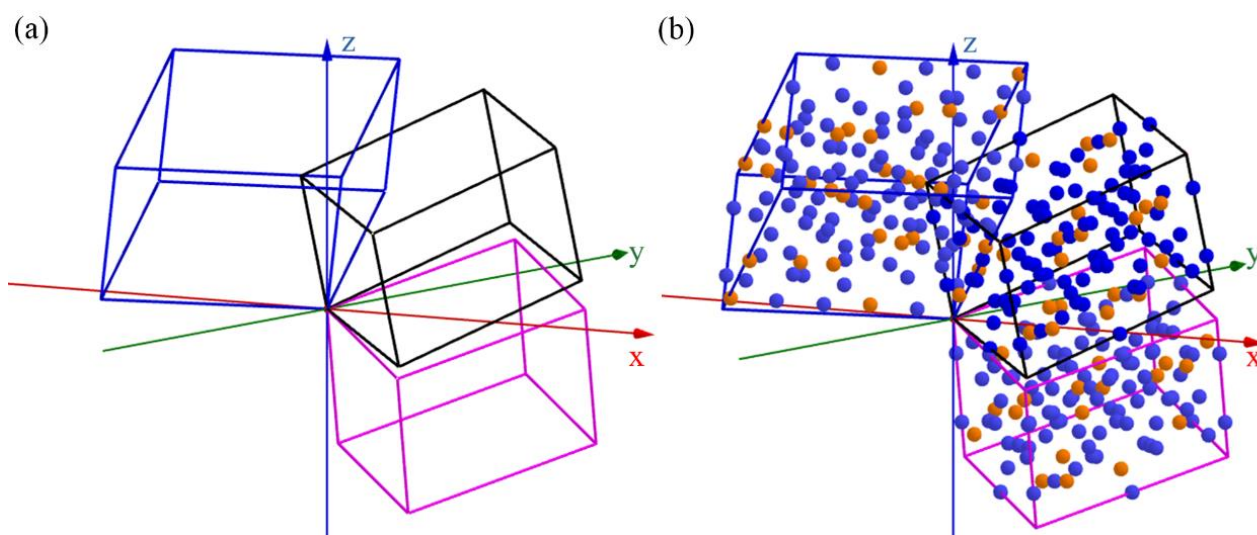


Figure 9. The structural models in real space for the $\text{Al}_{13}\text{Fe}_3$ and $\text{Al}_{13}\text{Fe}_4$ phases are presented: the orientation of cell edges (a) and the unit cell (b) (The saffron yellow atoms represent the Fe atoms and the blue atoms represent the Al atoms).

3.4. Interfaces between $\text{Al}_{13}\text{Fe}_3$ Phase and $\text{Al}_{13}\text{Fe}_4$ Phases

As described in the preceding section, the oriented structural models of the $\text{Al}_{13}\text{Fe}_3$ and $\text{Al}_{13}\text{Fe}_4$ phases were acquired. Nevertheless, the arrangement of atoms within the interfaces and the orientation of these interfaces remain ambiguous. To address these issues, the precession images obtained from the SXR D datasets were investigated, as depicted in Figures 10 and 11. All precession images were generated using a resolution of 0.85 \AA and a thickness of 0.02 \AA^{-1} .

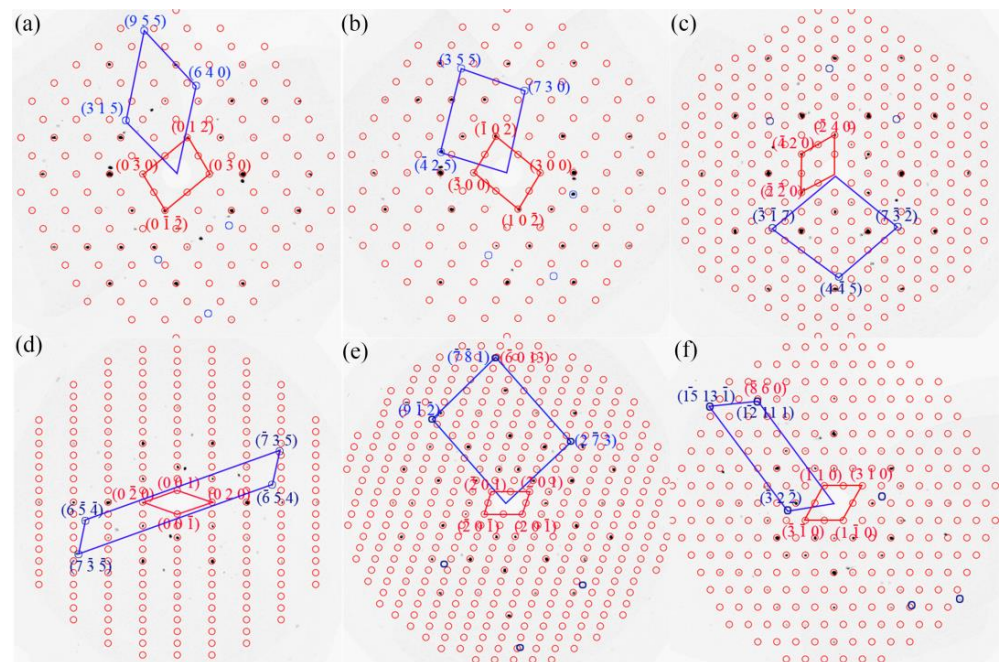


Figure 10. The precession images of intergrowth crystals are presented as follows: (a) $\text{Al}_{13}\text{Fe}_3\text{-}1(0kl)$, where the red and blue circles depict the crystal planes of the $\text{Al}_{13}\text{Fe}_3\text{-}1$ phase and $\text{Al}_{13}\text{Fe}_4$ phase, respectively. (b,c) show the same phase, with circles representing (b) $\text{Al}_{13}\text{Fe}_3\text{-}1(h0l)$ and (c) $\text{Al}_{13}\text{Fe}_3\text{-}1(hk0)$. Similarly, (d) $\text{Al}_{13}\text{Fe}_4(0kl)$ is shown, where the red and blue circles depict the crystal planes of the $\text{Al}_{13}\text{Fe}_4$ phase and $\text{Al}_{13}\text{Fe}_3\text{-}1$ phase, respectively. (e,f) show the same phase, with circles representing (e) $\text{Al}_{13}\text{Fe}_4(h0l)$ and (f) $\text{Al}_{13}\text{Fe}_4(hk0)$.

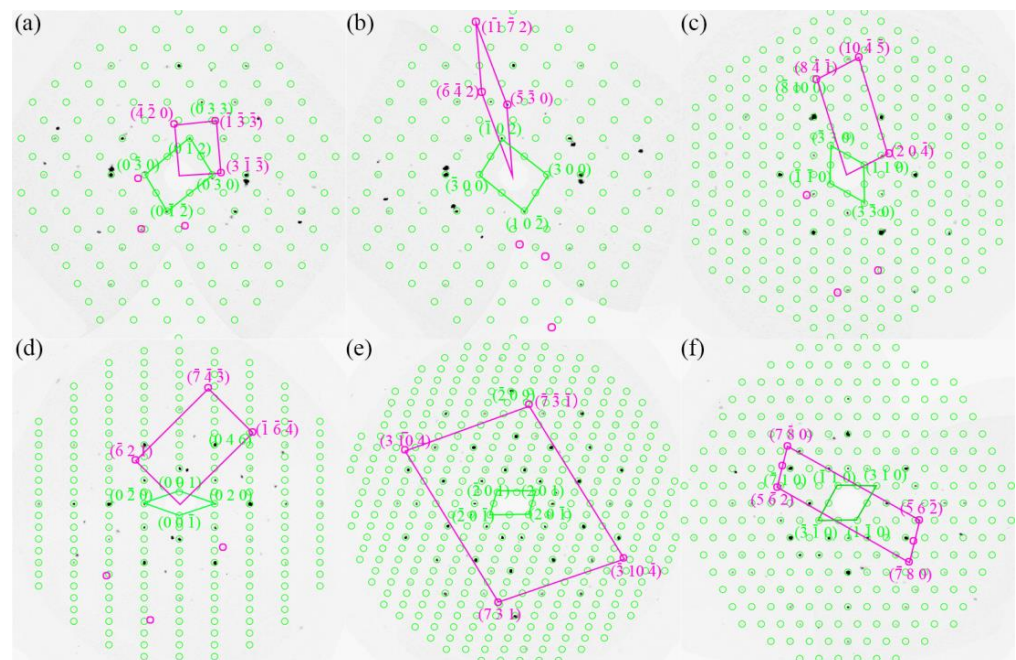


Figure 11. The precession images of intergrowth crystals are presented as follows: (a) $\text{Al}_{13}\text{Fe}_3\text{-}2(0kl)$, where the green and purple circles depict the crystal planes of the $\text{Al}_{13}\text{Fe}_3\text{-}2$ phase and $\text{Al}_{13}\text{Fe}_4$ phase, respectively. (b,c) show the same phase, with circles representing (b) $\text{Al}_{13}\text{Fe}_3\text{-}2(h0l)$ and (c) $\text{Al}_{13}\text{Fe}_3\text{-}2(hk0)$. Similarly, (d) $\text{Al}_{13}\text{Fe}_4(0kl)$ is shown, where the red and blue circles depict the crystal planes of the $\text{Al}_{13}\text{Fe}_4$ phase and $\text{Al}_{13}\text{Fe}_3\text{-}2$ phase, respectively. (e,f) show the same phase, with circles representing (e) $\text{Al}_{13}\text{Fe}_4(h0l)$ and (f) $\text{Al}_{13}\text{Fe}_4(hk0)$.

Figures 10 and 11 directly reveal the orientation relationships of the $Al_{13}Fe_3$ and $Al_{13}Fe_4$ phases represented by a pair of crystal planes. When two phases' diffraction spots overlap, it indicates that the crystal planes they represent are parallel. In summary, by examining Figure 10e,f and Figure 11a,c–f, which are displayed in Table 4, seven orientation relationships with the names OR1, OR2, OR3, OR4, OR5, OR6, and OR7 can be found. The seven orientation relationships between $Al_{13}Fe_3$ and $Al_{13}Fe_4$, as described in Table 4, are illustrated in a stereoscopic projection diagram for improved comprehension, as depicted in Figure 12.

Table 4. The seven crystallographic orientation relationships obtained from Figures 10 and 11 between $Al_{13}Fe_3$ and $Al_{13}Fe_4$.

	$[uvw]_{Al_{13}Fe_3} // [uvw]_{Al_{13}Fe_4}$	$(hkl)_{Al_{13}Fe_3} // (hkl)_{Al_{13}Fe_4}$
OR1	$[\bar{1}7\ 23\ 65]_{Al_{13}Fe_3} // [0\ 1\ 0]_{Al_{13}Fe_4}$	$(\bar{7}\bar{8}\ 1)_{Al_{13}Fe_3} // (\bar{6}\ 0\ 13)_{Al_{13}Fe_4}$
OR2	$[8\ 9\ 3]_{Al_{13}Fe_3} // [0\ 0\ 1]_{Al_{13}Fe_4}$	$(12\ 11\ 1)_{Al_{13}Fe_3} // (\bar{8}\ 6\ 0)_{Al_{13}Fe_4}$
OR3	$[1\ 0\ 0]_{Al_{13}Fe_3} // [3\ 6\ 5]_{Al_{13}Fe_4}$	$(0\ 3\ 3)_{Al_{13}Fe_3} // (\bar{1}\ \bar{3}\ \bar{3})_{Al_{13}Fe_4}$
OR4	$[0\ 0\ 1]_{Al_{13}Fe_3} // [8\ 15\ 4]_{Al_{13}Fe_4}$	$(\bar{8}\ 10\ 0)_{Al_{13}Fe_3} // (\bar{8}\ 4\ 1)_{Al_{13}Fe_4}$
OR5	$[\bar{2}2\bar{5}\ 38]_{Al_{13}Fe_3} // [1\ 0\ 0]_{Al_{13}Fe_4}$	$(1\ \bar{6}\ 4)_{Al_{13}Fe_3} // (0\ 4\ 6)_{Al_{13}Fe_4}$
OR6	$[\bar{2}2\ \bar{2}5\ \bar{7}9]_{Al_{13}Fe_3} // [0\ 1\ 0]_{Al_{13}Fe_4}$	$(\bar{7}\ \bar{3}\ \bar{1})_{Al_{13}Fe_3} // (\bar{2}\ 0\ 9)_{Al_{13}Fe_4}$
OR7	$[\bar{8}\ \bar{7}\ \bar{1}]_{Al_{13}Fe_3} // [0\ 0\ 1]_{Al_{13}Fe_4}$	$(5\ \bar{6}\ 2)_{Al_{13}Fe_3} // (\bar{7}\ 1\ 0)_{Al_{13}Fe_4}$

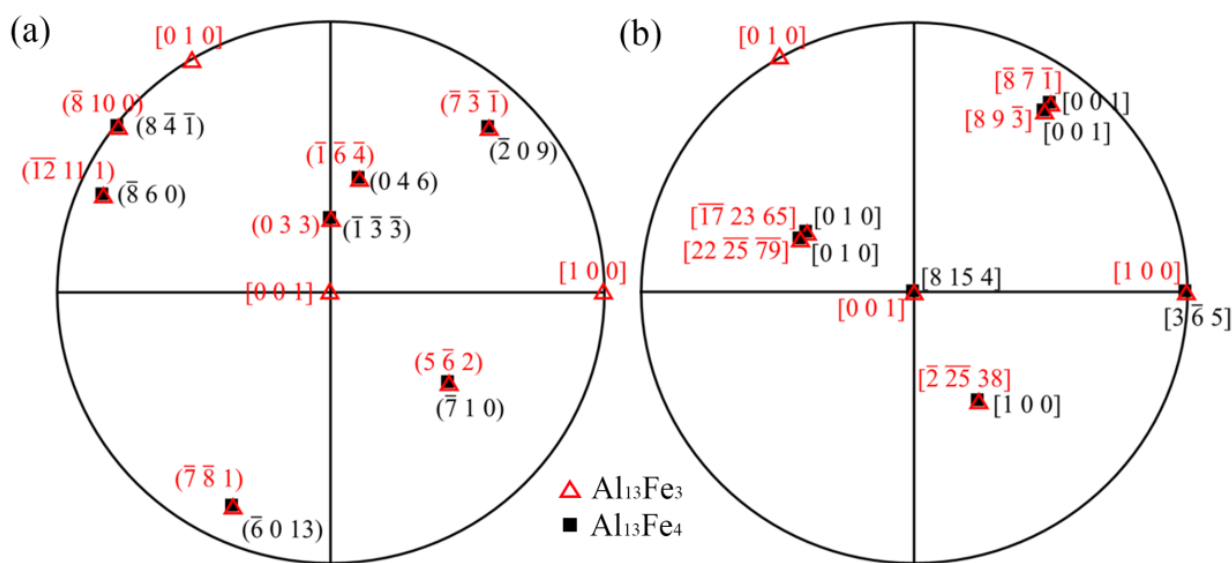


Figure 12. Stereographic projection of the orientation relationships between $Al_{13}Fe_3$ and $Al_{13}Fe_4$ based on the $Al_{13}Fe_3$ phase: (a) the orientation relationships between crystal planes, (b) the orientation relationships between crystal directions.

As mentioned above, seven crystallographic orientation relationships between the $Al_{13}Fe_3$ and $Al_{13}Fe_4$ phases can be identified from Figures 10 and 11. The crystallographic symmetry principle suggests that a set of orientation relationships found through experimentation usually correspond to many variations. Assessing the equivalence of the seven crystallographic orientation relationships found in the present study is crucial. The experiment data are analyzed and discussed using the matrix method in the following.

The matrix method involves determining the conversion correlation between the crystal plane index and the crystal direction index of two phases through mathematical analysis. A detailed description of the matrix method can be found in our group's prior research [52]. The conversion matrix between the seven orientation relationships can be obtained using this method, as demonstrated in Table 5 below, where matrix A represents

the conversion matrix between crystal planes, and matrix B represents the conversion matrix between crystal directions. It can be determined that there are seven independent orientation relationships because the elements in the conversion matrices corresponding to the seven orientation relationships have different absolute values.

Table 5. The conversion matrices between seven orientation relationships of Al₁₃Fe₃ and Al₁₃Fe₄ interfaces.

	Orientation Relationship	Conversion Matrix B	Conversion Matrix A
OR1	$(\bar{7}8\ 1)\text{Al}_{13}\text{Fe}_3 // (\bar{6}\ 0\ 13)\text{Al}_{13}\text{Fe}_4$ $[17\ 23\ 65]\text{Al}_{13}\text{Fe}_3 // [0\ 1\ 0]\text{Al}_{13}\text{Fe}_4$	$\begin{pmatrix} 0.90 & -0.19 & -0.80 \\ 0.11 & 0.26 & -0.88 \\ 1.22 & 0.74 & 0.28 \end{pmatrix}$	$\begin{pmatrix} 0.69 & -1.05 & -0.22 \\ -0.51 & 1.17 & -0.85 \\ 0.36 & 0.67 & 0.24 \end{pmatrix}$
OR2	$(\bar{1}2\ 11\ 1)\text{Al}_{13}\text{Fe}_3 // (\bar{8}\ 6\ 0)\text{Al}_{13}\text{Fe}_4$ $[8\ 9\ \bar{3}]\text{Al}_{13}\text{Fe}_3 // [0\ 0\ 1]\text{Al}_{13}\text{Fe}_4$	$\begin{pmatrix} -0.13 & -0.37 & 0.79 \\ -0.73 & 0.18 & 0.88 \\ -1.56 & -0.48 & -0.30 \end{pmatrix}$	$\begin{pmatrix} 0.35 & -1.51 & 0.61 \\ -0.47 & 1.20 & 0.50 \\ -0.45 & -0.44 & -0.28 \end{pmatrix}$
OR3	$(0\ 3\ 3)\text{Al}_{13}\text{Fe}_3 // (\bar{1}\ \bar{3}\ \bar{3})\text{Al}_{13}\text{Fe}_4$ $[1\ 0\ 0]\text{Al}_{13}\text{Fe}_3 // [3\ \bar{6}\ 5]\text{Al}_{13}\text{Fe}_4$	$\begin{pmatrix} 0.80 & -0.43 & 0.11 \\ 0.89 & -0.21 & -0.78 \\ -1.21 & -0.77 & -0.20 \end{pmatrix}$	$\begin{pmatrix} 0.54 & -1.08 & 0.90 \\ 0.16 & 0.02 & -1.09 \\ -0.35 & -0.70 & -0.21 \end{pmatrix}$
OR4	$(\bar{8}\ 10\ 0)\text{Al}_{13}\text{Fe}_3 // (841)\text{Al}_{13}\text{Fe}_4$ $[0\ 0\ 1]\text{Al}_{13}\text{Fe}_3 // [8\ 15\ 4]\text{Al}_{13}\text{Fe}_4$	$\begin{pmatrix} -0.60 & 0.07 & 0.96 \\ 0.32 & -0.35 & 0.67 \\ 1.29 & 0.75 & 0.12 \end{pmatrix}$	$\begin{pmatrix} -0.52 & 0.79 & 0.66 \\ 0.68 & -1.25 & 0.52 \\ 0.36 & 0.68 & 0.18 \end{pmatrix}$
OR5	$(\bar{1}\ \bar{6}\ 4)\text{Al}_{13}\text{Fe}_3 // (0\ 4\ 6)\text{Al}_{13}\text{Fe}_4$ $[225\ 38]\text{Al}_{13}\text{Fe}_3 // [1\ 0\ 0]\text{Al}_{13}\text{Fe}_4$	$\begin{pmatrix} -0.07 & -0.60 & 0.32 \\ -0.85 & -0.39 & -0.14 \\ 1.29 & -0.30 & -1.43 \end{pmatrix}$	$\begin{pmatrix} 0.50 & -1.33 & 0.73 \\ -0.91 & -0.30 & -0.76 \\ 0.20 & -0.27 & -0.46 \end{pmatrix}$
OR6	$(\bar{7}\ \bar{3}\ 1)\text{Al}_{13}\text{Fe}_3 // (\bar{2}\ 0\ 9)\text{Al}_{13}\text{Fe}_4$ $[22\ 25\ 79]\text{Al}_{13}\text{Fe}_3 // [0\ 1\ 0]\text{Al}_{13}\text{Fe}_4$	$\begin{pmatrix} 0.09 & 0.21 & -0.91 \\ 0.86 & -0.23 & -0.78 \\ -1.28 & -0.75 & -0.15 \end{pmatrix}$	$\begin{pmatrix} -0.52 & 1.08 & -0.91 \\ 0.68 & -1.12 & -0.19 \\ -0.36 & -0.68 & -0.19 \end{pmatrix}$
OR7	$(5\ \bar{6}\ 2)\text{Al}_{13}\text{Fe}_3 // (\bar{7}\ 1\ 0)\text{Al}_{13}\text{Fe}_4$ $[8\ \bar{7}\ 1]\text{Al}_{13}\text{Fe}_3 // [0\ 0\ 1]\text{Al}_{13}\text{Fe}_4$	$\begin{pmatrix} 0.07 & 0.21 & -0.90 \\ 0.83 & -0.25 & -0.79 \\ -1.32 & -0.74 & -0.11 \end{pmatrix}$	$\begin{pmatrix} -0.53 & 1.09 & -0.90 \\ 0.66 & -1.15 & -0.21 \\ -0.37 & -0.67 & -0.18 \end{pmatrix}$

Moreover, an elementary model of the interface relationship was established, using the OR3 orientation relationship as an example. Specifically, the (033) surface of Al₁₃Fe₃ was considered, with the *u* and *v* directions aligned with [100] and [011], respectively (as depicted in Figure 13a). The lattice parameters of this surface were found to be *u* = 14.596 Å, *v* = 16.499 Å, and $\theta = 116.252^\circ$. In contrast, the surface of ($\bar{1}\bar{3}\bar{3}$) Al₁₃Fe₄ was modeled with the *u* and *v* directions aligned with [365] and [310], respectively (as shown in Figure 13b). The lattice parameters of this surface were determined to be *u* = 81.472 Å, *v* = 47.191 Å, and $\theta = 115.688^\circ$. Due to the significant mismatch between the (033) surface of Al₁₃Fe₃ and the ($\bar{1}\bar{3}\bar{3}$) surface of Al₁₃Fe₄ in the *u* and *v* directions, a supercell interface model must be constructed to satisfy the periodic boundary conditions. To reduce mismatches when constructing large supercells, relatively small mismatches can be achieved using 6(*u*) × 3(*v*) (033) Al₁₃Fe₃ and 1(*u*) × 1(*v*) ($\bar{1}\bar{3}\bar{3}$) Al₁₃Fe₄ surface models, resulting in $\delta(u) = 6.97\%$ and $\delta(v) = 4.66\%$ mismatches in the *u* and *v* directions, respectively. Figure 13c displays the atomic interface model of Al₁₃Fe₃(033)/Al₁₃Fe₄($\bar{1}\bar{3}\bar{3}$).

As can be seen from Figure 13, the surface of Al₁₃Fe₃(033) is composed of 63 Al atoms, while the surface of Al₁₃Fe₄($\bar{1}\bar{3}\bar{3}$) is composed of 111 atoms, including 20 Fe atoms and 91 Al atoms.

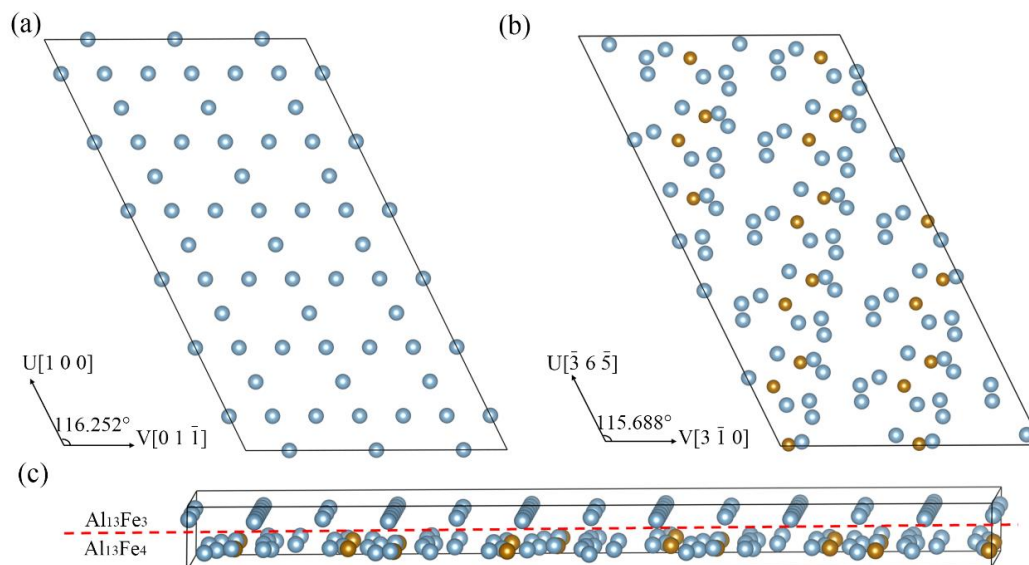


Figure 13. (a): (033) surface of the $\text{Al}_{13}\text{Fe}_3$ phase; (b): $(\bar{1}\bar{3}\bar{3})$ surface of the $\text{Al}_{13}\text{Fe}_4$ phase; (c): the atomic interface model of $\text{Al}_{13}\text{Fe}_3(033)/\text{Al}_{13}\text{Fe}_4(\bar{1}\bar{3}\bar{3})$ (The golden atoms represent the Fe atoms and the blue atoms represent the Al atoms).

4. Conclusions

In summary, two typical approximate quasicrystalline phases $\text{Al}_{13}\text{Fe}_3$ and $\text{Al}_{13}\text{Fe}_4$ in the Al-Fe binary system were discovered to be intergrowth as a single crystal with a size of tens of micrometers, which was characterized by SXR D by combining SEM and EDX analysis. The first phase is refined to $\text{Al}_{13}\text{Fe}_3$ (space group $R\bar{3}c$) with cell parameters $a = b = 14.5956(9)$ Å, $c = 7.6929(4)$ Å, $\alpha = \beta = 90^\circ$, and $\gamma = 120^\circ$. The second phase is refined to $\text{Al}_{13}\text{Fe}_4$ (space group $C2/m$) with cell parameters: $a = 15.498(4)$ Å, $b = 8.0814(17)$ Å, $c = 12.488(3)$ Å, $\beta = 107.790(8)^\circ$. All atoms in these two phases are fully occupied. Topological analysis reveals that both phases have distorted icosahedrons as structural building units. Furthermore, structural models for coexistence of the $\text{Al}_{13}\text{Fe}_3$ and $\text{Al}_{13}\text{Fe}_4$ phases were obtained from analyzing the SXR D datasets in reciprocal space as well as the refined three models in real space.

The crystallographic orientation relationships of interfaces between the $\text{Al}_{13}\text{Fe}_3$ and $\text{Al}_{13}\text{Fe}_4$ phases were built by studying the synthesized precession planes from the SXR D datasets. Seven orientation relationships (named OR1 to OR7) were found by analyzing the $(0kl)$, $(h0l)$, and $(hk0)$ planes of these phases. The distribution of atoms inside the interfaces is illustrated with a preliminary interface model of OR3.

The present research provides a protocol for analyzing the detailed crystal structures of three intergrowth phases and investigating their orientation relationships as well as interfaces between intergrowth phases, which will definitely stimulate further related works involving advanced scanning and transmission electron microscopy techniques and will shed light on clarifying the mechanism of multi-growth samples that are frequently found in the complex metallic alloys.

Supplementary Materials: The following supporting information can be downloaded at: <https://www.mdpi.com/article/10.3390/met14040463/s1>. The Supplementary Materials contain a stereographic projection illustrating the orientation relationships between $\text{Al}_{13}\text{Fe}_3$ and $\text{Al}_{13}\text{Fe}_4$, as well as SEM and EDX analysis of the single crystal sample. Additionally, precession images of the $(1kl)$, $(h1l)$, and $(hk1)$ planes to $(5kl)$, $(h5l)$, and $(hk5)$ planes are provided. Figure S1: scanning electron microscope (SEM) micrographs of single crystal sample. EDX analysis was performed for various locations as indicated in Table S1. Table S1: The EDX results conducted at every scanning location. Figure S2: The precession images of (a) $\text{Al}_{13}\text{Fe}_3$ -1($0kl$), (b) $\text{Al}_{13}\text{Fe}_3$ -1($h0l$), (c) $\text{Al}_{13}\text{Fe}_3$ -1($hk0$), (d) $\text{Al}_{13}\text{Fe}_4$ ($0kl$), (e) $\text{Al}_{13}\text{Fe}_4$ ($h0l$), (f) $\text{Al}_{13}\text{Fe}_4$ ($hk0$); Figure S3: The precession images of intergrowth

crystals: (a) $\text{Al}_{13}\text{Fe}_3\text{-}2(0kl)$, (b) $\text{Al}_{13}\text{Fe}_3\text{-}2(h0l)$, (c) $\text{Al}_{13}\text{Fe}_3\text{-}2(hk0)$, (d) $\text{Al}_{13}\text{Fe}_4(0kl)$, (e) $\text{Al}_{13}\text{Fe}_4(h0l)$, (f) $\text{Al}_{13}\text{Fe}_4(hk0)$. Figure S4: The precession images of (a) $\text{Al}_{13}\text{Fe}_3\text{-}1(1kl)$, (b) $\text{Al}_{13}\text{Fe}_3\text{-}1(h1l)$, (c) $\text{Al}_{13}\text{Fe}_3\text{-}1(hk1)$, (d) $\text{Al}_{13}\text{Fe}_4(1kl)$, (e) $\text{Al}_{13}\text{Fe}_4(h1l)$, (f) $\text{Al}_{13}\text{Fe}_4(hk1)$. Figure S5: The precession images of (a) $\text{Al}_{13}\text{Fe}_3\text{-}1(2kl)$, (b) $\text{Al}_{13}\text{Fe}_3\text{-}1(h2l)$, (c) $\text{Al}_{13}\text{Fe}_3\text{-}1(hk2)$, (d) $\text{Al}_{13}\text{Fe}_4(2kl)$, (e) $\text{Al}_{13}\text{Fe}_4(h2l)$, (f) $\text{Al}_{13}\text{Fe}_4(hk2)$. Figure S6: The precession images of (a) $\text{Al}_{13}\text{Fe}_3\text{-}1(3kl)$, (b) $\text{Al}_{13}\text{Fe}_3\text{-}1(h3l)$, (c) $\text{Al}_{13}\text{Fe}_3\text{-}1(hk3)$, (d) $\text{Al}_{13}\text{Fe}_4(3kl)$, (e) $\text{Al}_{13}\text{Fe}_4(h3l)$, (f) $\text{Al}_{13}\text{Fe}_4(hk3)$. Figure S7: The precession images of (a) $\text{Al}_{13}\text{Fe}_3\text{-}1(4kl)$, (b) $\text{Al}_{13}\text{Fe}_3\text{-}1(h4l)$, (c) $\text{Al}_{13}\text{Fe}_3\text{-}1(hk4)$, (d) $\text{Al}_{13}\text{Fe}_4(4kl)$, (e) $\text{Al}_{13}\text{Fe}_4(h4l)$, (f) $\text{Al}_{13}\text{Fe}_4(hk4)$. Figure S8: The precession images of (a) $\text{Al}_{13}\text{Fe}_3\text{-}1(5kl)$, (b) $\text{Al}_{13}\text{Fe}_3\text{-}1(h5l)$, (c) $\text{Al}_{13}\text{Fe}_3\text{-}1(hk5)$, (d) $\text{Al}_{13}\text{Fe}_4(5kl)$, (e) $\text{Al}_{13}\text{Fe}_4(h5l)$, (f) $\text{Al}_{13}\text{Fe}_4(hk5)$. Figure S9: The precession images of (a) $\text{Al}_{13}\text{Fe}_3\text{-}2(1kl)$, (b) $\text{Al}_{13}\text{Fe}_3\text{-}2(h1l)$, (c) $\text{Al}_{13}\text{Fe}_3\text{-}2(hk1)$, (d) $\text{Al}_{13}\text{Fe}_4(1kl)$, (e) $\text{Al}_{13}\text{Fe}_4(h1l)$, (f) $\text{Al}_{13}\text{Fe}_4(hk1)$. Figure S10: The precession images of (a) $\text{Al}_{13}\text{Fe}_3\text{-}2(2kl)$, (b) $\text{Al}_{13}\text{Fe}_3\text{-}2(h2l)$, (c) $\text{Al}_{13}\text{Fe}_3\text{-}2(hk2)$, (d) $\text{Al}_{13}\text{Fe}_4(2kl)$, (e) $\text{Al}_{13}\text{Fe}_4(h2l)$, (f) $\text{Al}_{13}\text{Fe}_4(hk2)$. Figure S11: The precession images of (a) $\text{Al}_{13}\text{Fe}_3\text{-}2(3kl)$, (b) $\text{Al}_{13}\text{Fe}_3\text{-}2(h3l)$, (c) $\text{Al}_{13}\text{Fe}_3\text{-}2(hk3)$, (d) $\text{Al}_{13}\text{Fe}_4(3kl)$, (e) $\text{Al}_{13}\text{Fe}_4(h3l)$, (f) $\text{Al}_{13}\text{Fe}_4(hk3)$. Figure S12: The precession images of (a) $\text{Al}_{13}\text{Fe}_3\text{-}2(4kl)$, (b) $\text{Al}_{13}\text{Fe}_3\text{-}2(h4l)$, (c) $\text{Al}_{13}\text{Fe}_3\text{-}2(hk4)$, (d) $\text{Al}_{13}\text{Fe}_4(4kl)$, (e) $\text{Al}_{13}\text{Fe}_4(h4l)$, (f) $\text{Al}_{13}\text{Fe}_4(hk4)$. Figure S13: The precession images of (a) $\text{Al}_{13}\text{Fe}_3\text{-}2(5kl)$, (b) $\text{Al}_{13}\text{Fe}_3\text{-}2(h5l)$, (c) $\text{Al}_{13}\text{Fe}_3\text{-}2(hk5)$, (d) $\text{Al}_{13}\text{Fe}_4(5kl)$, (e) $\text{Al}_{13}\text{Fe}_4(h5l)$, (f) $\text{Al}_{13}\text{Fe}_4(hk5)$.

Author Contributions: Conceptualization, C.F., R.F., B.W. and L.Z.; methodology, C.F.; investigation, Y.L. and Z.X.; resources, C.F., Z.X. and L.Z.; writing—original draft preparation, Y.L.; writing—review and editing, C.F., Z.X., R.F., B.W. and L.Z.; supervision, C.F., R.F. and L.Z.; funding acquisition, C.F., Z.X. and B.W. All authors have read and agreed to the published version of the manuscript.

Funding: This research was funded by the National Natural Science Foundation of China (grant No. 52173231; grant No. 51925105), Hebei Natural Science Foundation (grant No. E2022203182; grant No. E2020203158), Project of Hebei Provincial Department of Human Resources and Social Security (grant No. E2020100006), and Innovation Ability Promotion Project of Hebei supported by Hebei Key Lab for Optimizing Metal Product Technology and Performance (grant No. 22567609H).

Data Availability Statement: Data will be made available on request.

Acknowledgments: The authors express their gratitude to Qiang Ren from the High Steel Center at Yanshan University for providing support in conducting the SEM/EDX measurements.

Conflicts of Interest: The authors declare no conflicts of interest.

Appendix A

During the processing of data, the orientation matrix plays a crucial role as it is a 3×3 matrix that specifies the values and orientations of the three reciprocal axes based on the x , y , and z coordinates on the goniometer. This matrix holds the fundamental information that defines the reciprocal cell and its spatial orientation. In reciprocal space, the orientation matrix can be characterized as:

$$R = \begin{pmatrix} a_x^* & b_x^* & c_x^* \\ a_y^* & b_y^* & c_y^* \\ a_z^* & b_z^* & c_z^* \end{pmatrix} \quad (\text{A1})$$

where a_x^* , a_y^* , and a_z^* represent the coordinate components of the reciprocity vector a^* in the x , y , and z directions, respectively, based on the diffractometer coordinates. Similarly, the second and third columns represent the coordinate components of b^* and c^* , respectively.

According to Section 3.1, we know there are two sets of $\text{Al}_{13}\text{Fe}_3$. Now, the gray diffraction point corresponds to the $\text{Al}_{13}\text{Fe}_3\text{-}1$ phase and the yellow diffraction point corresponds to the $\text{Al}_{13}\text{Fe}_3\text{-}2$ phase. The orientation matrix of the $\text{Al}_{13}\text{Fe}_3\text{-}1$ phase, $\text{Al}_{13}\text{Fe}_3\text{-}2$ phase, and $\text{Al}_{13}\text{Fe}_4$ phase in reciprocal space can be found using the APEX3 software, where the orientation matrix in reciprocal space of the $\text{Al}_{13}\text{Fe}_3\text{-}1$ phase is:

$$\begin{pmatrix} +0.07726900 & +0.05223162 & -0.00936381 \\ -0.01660753 & +0.05673444 & -0.03000876 \\ +0.00178704 & +0.01739432 & +0.12599610 \end{pmatrix} \quad (\text{A2})$$

The orientation matrix in reciprocal space of the $\text{Al}_{13}\text{Fe}_3$ -2 phase is:

$$\begin{pmatrix} +0.5312165 & +0.07719827 & -0.00363642 \\ +0.05774164 & -0.01607857 & +0.02432341 \\ +0.00946710 & -0.00524772 & -0.12749440 \end{pmatrix} \quad (\text{A3})$$

The orientation matrix in reciprocal space of the $\text{Al}_{13}\text{Fe}_4$ phase is:

$$\begin{pmatrix} +0.02463529 & -0.02672067 & -0.06323070 \\ -0.05067153 & +0.06340674 & -0.05297208 \\ +0.03764391 & +0.10283705 & +0.01623344 \end{pmatrix} \quad (\text{A4})$$

Starting from the fundamental correspondence between real space and reciprocal space:

$$a \cdot a^* = b \cdot b^* = c \cdot c^* = 1 \quad (\text{A5})$$

The orientation matrix of these three phases in real space can be derived. The orientation matrix in real space of the $\text{Al}_{13}\text{Fe}_3$ -1 phase is:

$$\begin{pmatrix} +10.91316436 & -9.59578453 & -1.47479968 \\ +2.90159188 & +13.87577253 & +3.52064947 \\ -0.55511139 & -1.77963193 & 7.47148199 \end{pmatrix} \quad (\text{A6})$$

The orientation matrix in real space of the $\text{Al}_{13}\text{Fe}_3$ -2 phase is:

$$\begin{pmatrix} +3.10098452 & +14.06396551 & +2.58737191 \\ +10.82854274 & -9.60619433 & -2.13761384 \\ -0.216569920 & +1.44058379 & -7.57090465 \end{pmatrix} \quad (\text{A7})$$

The orientation matrix in real space of the $\text{Al}_{13}\text{Fe}_4$ phase is:

$$\begin{pmatrix} +9.64924243 & -9.04020620 & +8.08117528 \\ -1.74532373 & +4.14156070 & +6.71704330 \\ -11.31930567 & -5.27289202 & +0.30998032 \end{pmatrix} \quad (\text{A8})$$

It is achievable to build complete models of $\text{Al}_{13}\text{Fe}_3$ -1, $\text{Al}_{13}\text{Fe}_3$ -2, and $\text{Al}_{13}\text{Fe}_4$ described with cell edges in real space utilizing the orientation matrix for those phases in real space. as displayed in the main text's Figure 9a.

By recognizing the experiment's orientation matrix and the orientation matrix associated with the Crystallographic Information File (CIF), the particular atoms for both phases to the orientation models described with cell edges can be added. First, the real-space locations of the $\text{Al}_{13}\text{Fe}_4$ phase's atoms are introduced. We designated matrix B as the experimental orientation matrix of the phase in real space. The $\text{Al}_{13}\text{Fe}_4$ -related CIF-related orientation matrix is defined as follows:

$$A = \begin{pmatrix} 15.49800015 & 0 & 0 \\ 0 & 8.08139992 & 0 \\ -3.81544784 & 0 & 11.89085782 \end{pmatrix} \quad (\text{A9})$$

By utilizing matrix A and matrix B, it is possible to establish the transformation relationship between the two matrices. By setting $AC = B$, we can solve for matrix C:

$$C = \begin{pmatrix} +0.62261210 & -0.58331437 & +0.52143342 \\ -0.21596799 & +0.51248060 & +0.83117323 \\ -0.75215445 & -0.63061031 & +0.19338238 \end{pmatrix} \quad (\text{A10})$$

The CIF of $\text{Al}_{13}\text{Fe}_4$ contains the Cartesian coordinates of its atoms, which are then transformed into the corresponding positions in real space by multiplying them with matrix C:

C. This process is also applied to obtain the coordinate positions of the atoms in the $\text{Al}_{13}\text{Fe}_3-1$ and $\text{Al}_{13}\text{Fe}_3-2$ phases. By following this procedure, comprehensive oriented structural models of the $\text{Al}_{13}\text{Fe}_3-1$, $\text{Al}_{13}\text{Fe}_3-2$, and $\text{Al}_{13}\text{Fe}_4$ phases in real space were obtained and are presented in Figure 9b of the main text.

References

1. Tcherdyntsev, V.V.; Kaloshkin, S.D.; Gunderov, D.V.; Afonina, E.A.; Brodova, I.G.; Stolyarov, V.V.; Baldokhin, Y.V.; Shelekhov, E.V.; Tomilin, I.A. Phase composition and microhardness of rapidly quenched Al–Fe alloys after high pressure torsion deformation. *Mater. Sci. Eng. A* **2004**, *375*, 888–893. [[CrossRef](#)]
2. Sasaki, T.T.; Ohkubo, T.; Hono, K. Microstructure and mechanical properties of bulk nanocrystalline Al–Fe alloy processed by mechanical alloying and spark plasma sintering. *Acta Mater.* **2009**, *57*, 3529–3538. [[CrossRef](#)]
3. Goulart, P.R.; Spinelli, J.E.; Cheung, N.; Garcia, A. The effects of cell spacing and distribution of intermetallic fibers on the mechanical properties of hypoeutectic Al–Fe alloys. *Mater. Chem. Phys.* **2010**, *119*, 272–278. [[CrossRef](#)]
4. Akinlade, O.; Singh, R.N.; Sommer, F. Thermodynamics of liquid Al–Fe alloys. *J. Alloys Compd.* **2000**, *299*, 163–168. [[CrossRef](#)]
5. Pariona, M.M.; Teleginski, V.; Santos, K.D.; Machado, S.; Zara, A.J.; Zurba, N.K.; Riva, R. Yb-fiber laser beam effects on the surface modification of Al–Fe aerospace alloy obtaining weld filet structures, low fine porosity and corrosion resistance. *Surf. Coat. Technol.* **2012**, *206*, 2293–2301. [[CrossRef](#)]
6. Staley, J.T.; Liu, J.; Hunt, W.H., Jr. Aluminum alloys for aerostructures. *Adv. Mater. Process.* **1997**, *152*, 17–21.
7. Zhou, B.; Liu, B.; Zhang, S. The advancement of 7xxx series aluminum alloys for aircraft structures: A review. *Metals* **2021**, *11*, 718. [[CrossRef](#)]
8. Pariona, M.M.; Teleginski, V.; dos Santos, K.; dos Santos, E.L.R.; Riva, R. AFM study of the effects of laser surface remelting on the morphology of Al–Fe aerospace alloys. *Mater. Charact.* **2012**, *74*, 64–76. [[CrossRef](#)]
9. Pariona, M.M.; Teleginski, V.; dos Santos, K.; de Lima, A.A.; Zara, A.J.; Micene, K.T.; Riva, R. Influence of laser surface treated on the characterization and corrosion behavior of Al–Fe aerospace alloys. *Appl. Surf. Sci.* **2013**, *276*, 76–85. [[CrossRef](#)]
10. Simon, P.; Beggs, P.D. A numerical performance comparison of a dual-phase steel and aluminium alloy bumper bar system. *Int. J. Crashworthiness* **2010**, *15*, 425–442. [[CrossRef](#)]
11. Hirsch, J. Recent development in aluminium for automotive applications. *Trans. Nonferrous Met. Soc. China* **2014**, *24*, 1995–2002. [[CrossRef](#)]
12. Karim, M.A.; Park, Y.D. A review on welding of dissimilar metals in car body manufacturing. *J. Weld. Join.* **2020**, *38*, 8–23. [[CrossRef](#)]
13. Park, K.; Park, J.; Kwon, H. Fabrication and characterization of Al–SUS316L composite materials manufactured by the spark plasma sintering process. *Mater. Sci. Eng. A* **2017**, *691*, 8–15. [[CrossRef](#)]
14. Mukai, T.; Suresh, S.; Kita, K.; Sasaki, H.; Kobayashi, N.; Higashi, K.; Inoue, A. Nanostructured Al–Fe alloys produced by e-beam deposition: Static and dynamic tensile properties. *Acta Mater.* **2003**, *51*, 4197–4208. [[CrossRef](#)]
15. Liang, D.; Jie, W.; Jones, H. The effect of growth velocity on primary spacing of Al_3Fe dendrites in hypereutectic Al–Fe alloys. *J. Cryst. Growth* **1994**, *135*, 561–564. [[CrossRef](#)]
16. Senkov, O.N.; Froes, F.H.; Stolyarov, V.V.; Valiev, R.Z.; Liu, J. Microstructure of aluminum-iron alloys subjected to severe plastic deformation. *Scr. Mater.* **1998**, *38*, 1511–1516. [[CrossRef](#)]
17. Medvedev, A.; Murashkin, M.; Enikeev, N.; Medvedev, E.; Sauvage, X. Influence of morphology of intermetallic particles on the microstructure and properties evolution in severely deformed Al–Fe alloys. *Metals* **2021**, *11*, 815. [[CrossRef](#)]
18. Luo, S.X.; Shi, Z.M.; Li, N.Y.; Lin, Y.M.; Liang, Y.H.; Zeng, Y.D. Crystallization inhibition and microstructure refinement of Al–5Fe alloys by addition of rare earth elements. *J. Alloys Compd.* **2019**, *789*, 90–99. [[CrossRef](#)]
19. Duchaussoy, A.; Sauvage, X.; Edalati, K.; Horita, Z.; Renou, G.; Deschamps, A.; De Geuser, F. Structure and mechanical behavior of ultrafine-grained aluminum-iron alloy stabilized by nanoscaled intermetallic particles. *Acta Mater.* **2019**, *167*, 89–102. [[CrossRef](#)]
20. Guan, R.G.; Tie, D. A review on grain refinement of aluminum alloys: Progresses, challenges and prospects. *Acta Metall. Sin.* **2017**, *30*, 409–432. [[CrossRef](#)]
21. Cubero-Sesin, J.M.; Horita, Z. Strengthening via Microstructure Refinement in Bulk Al–4 mass% Fe Alloy Using High-Pressure Torsion. *Mater. Trans.* **2012**, *53*, 46–55. [[CrossRef](#)]
22. Fung, K.K.; Yang, C.Y.; Zhou, Y.Q.; Zhao, J.G.; Zhan, W.S.; Shen, B.G. Icosahedrally related decagonal quasicrystal in rapidly cooled Al–14-at.%-Fe alloy. *Phys. Rev. Lett.* **1986**, *56*, 2060–2063. [[CrossRef](#)] [[PubMed](#)]
23. Cairney, J.M.; Munroe, P.R.; Sordelet, D.J. Microstructural analysis of a FeAl/quasicrystal-based composite prepared using a focused ion beam miller. *J. Microsc.* **2001**, *201*, 201–211. [[CrossRef](#)]
24. Liu, Y.; Liu, H.; Fan, C.; Wen, B.; Zhang, L. Crystal structure of $\text{AlFe}_{0.95}$. *IUCrData* **2023**, *8*, x231065. [[CrossRef](#)]
25. Stein, F.; Vogel, S.C.; Eumann, M.; Palm, M. Determination of the crystal structure of the ϵ phase in the Fe–Al system by high-temperature neutron diffraction. *Intermetallics* **2010**, *18*, 150–156. [[CrossRef](#)]
26. Burkhardt, U.; Grin, Y.; Ellner, M.; Peters, K. Structure refinement of the iron–aluminium phase with the approximate composition Fe_2Al_5 . *Acta Crystallogr. B Struct. Sci.* **1994**, *50*, 313–316. [[CrossRef](#)]
27. Chumak, I.; Richter, K.W.; Ehrenberg, H. Redetermination of iron dialuminide, FeAl_2 . *Acta Crystallogr. C* **2010**, *66*, i87–i88. [[CrossRef](#)] [[PubMed](#)]

28. Grin, J.; Burkhardt, U.; Ellner, M.; Peters, K. Refinement of the $\text{Fe}_4\text{Al}_{13}$ structure and its relationship to the quasihomological homeotypical structures. *Z Krist. Cryst. Mater.* **1994**, *209*, 479–487. [[CrossRef](#)]
29. Xia, Z.; Liu, C.; Fan, C. $\text{Al}_{13}\text{Fe}_3$. *IUCrData* **2018**, *3*, x180593. [[CrossRef](#)]
30. Black, P.J. The structure of FeAl_3 . II. *Acta Crystallogr.* **1955**, *8*, 175–182. [[CrossRef](#)]
31. Saitoh, K.; Yokosawa, T.; Tanaka, M.; Tsai, A.P. Structural studies of monoclinic approximants of $\text{Al}_{13}\text{Fe}_4$ and τ -inflated $\text{Al}_{13}\text{Co}_4$ by the high-angle annular dark-field method. *Microscopy* **1999**, *48*, 105–114.
32. Yanson, T.I.; Manyako, N.B.; Bodak, O.I.; Cerny, R.; Gladyshevskii, R.E.; Yvon, K. Crystal structure of $\text{Fe}_4\text{Ti}_{0.93}\text{Al}_{12.07}$, a substitutional variant of the $\text{Fe}_4\text{Al}_{13}$ structure type. *J. Alloys Compd.* **1995**, *219*, 135–138. [[CrossRef](#)]
33. Popčević, P.; Smontara, A.; Ivkov, J.; Wencka, M.; Komelj, M.; Jeglic, P.; Vrtnik, S.; Bobnar, M.; Jaglicic, Z.; Bauer, B.; et al. Anisotropic physical properties of the $\text{Al}_{13}\text{Fe}_4$ complex intermetallic and its ternary derivative $\text{Al}_{13}(\text{Fe},\text{Ni})_4$. *Phys. Rev. B* **2010**, *81*, 184203. [[CrossRef](#)]
34. Liu, C.; Fan, C. Crystal structure of the λ - $\text{Al}_{13}\text{Fe}_4$ -type intermetallic $(\text{Al},\text{Cu})_{13}(\text{Fe},\text{Cu})_4$. *IUCrData* **2018**, *3*, x180363. [[CrossRef](#)]
35. Barbier, J.N.; Tamura, N.; Verger-Gaugry, J.L. Monoclinic $\text{Al}_{13}\text{Fe}_4$ approximant phase: A link between icosahedral and decagonal phases. *J. Non. Cryst. Solids.* **1993**, *153*, 126–131. [[CrossRef](#)]
36. Osawa, A.; Murata, T. On the equilibrium diagram of iron-aluminium system. *Sci. Rep. Tohoku Univ.* **1933**, *22*, 803–823.
37. Phragmen, G. On the phases occurring in alloys of aluminium with copper, magnesium, manganese, iron, and silicon. *J. Inst. Met.* **1950**, *77*, 489–551.
38. Black, P.J. The structure of FeAl_3 . I. *Acta Crystallogr.* **1955**, *8*, 43–48. [[CrossRef](#)]
39. Ma, X.L.; Liebertz, H.; Köster, U. Multiple Twins of Monoclinic $\text{Al}_{13}\text{Fe}_4$ Showing Pseudo-Orthorhombic and Fivefold Symmetries. *Phys. Status Solidi A* **1996**, *158*, 359–367. [[CrossRef](#)]
40. Griger, A.; Stefániay, V.; Turmezey, T. Crystallographic data and chemical compositions of aluminium-rich Al-Fe intermetallic phases. *Int. J. Mater. Res.* **1986**, *77*, 30–35. [[CrossRef](#)]
41. Chandrasekaran, M.; Lin, Y.P.; Vincent, R.; Staniek, G. The structure and stability of some intermetallic phases in rapidly solidified AlFe. *Scr. Metall.* **1988**, *22*, 797–802. [[CrossRef](#)]
42. Tsuchimori, M.; Ishimasa, T.; Fukano, Y. Crystal structures of small Al-rich Fe alloy particles formed by a gas-evaporation technique. *Philos. Mag. B* **1992**, *66*, 89–108. [[CrossRef](#)]
43. Lafaye, P.; Oishi, K.; Bourdon, M.; Harvey, J.P. Crystal chemistry and thermodynamic modelling of the $\text{Al}_{13}(\text{Fe},\text{TM})_4$ solid solutions (TM = Co, Cr, Ni, Pt). *J. Alloys Compd.* **2022**, *920*, 165779. [[CrossRef](#)]
44. Lafaye, P.; Oishi, K.; Harvey, J.P. A comprehensive study on the thermodynamics of the $\text{Al}_{13}\text{Fe}_4$ solid solution in the Al-Fe-Mn ternary system. *J. Alloys Compd.* **2023**, *944*, 169054. [[CrossRef](#)]
45. Sharma, A.; Morisada, Y.; Ushioda, K.; Fujii, H. Elucidation on the correlation between thermal stability of $\text{Al}_{13}\text{Fe}_4$ intermetallic phase and mechanical properties of the Al-Fe alloy fabricated via friction stir alloying. *J. Alloys Compd.* **2023**, *967*, 171732. [[CrossRef](#)]
46. Cui, Y.; Gourlay, C.M. Growth twinning and morphology of $\text{Al}_{45}\text{Cr}_7$ and $\text{Al}_{13}\text{Fe}_4$. *J. Alloys Compd.* **2022**, *893*, 162318. [[CrossRef](#)]
47. Pang, N.; Shi, Z.; Wang, C.; Li, N.; Lin, Y. Influence of Cr, Mn, Co and Ni Addition on Crystallization Behavior of $\text{Al}_{13}\text{Fe}_4$ Phase in Al-5Fe Alloys Based on ThermoDynamic Calculations. *Materials* **2021**, *14*, 768. [[CrossRef](#)]
48. Song, Z.; Magdysyuk, O.V.; Tang, L.; Sparks, T.; Cai, B. Growth dynamics of faceted $\text{Al}_{13}\text{Fe}_4$ intermetallic revealed by high-speed synchrotron X-ray quantification. *J. Alloys Compd.* **2021**, *861*, 158604. [[CrossRef](#)]
49. Sahu, M.; Paul, A.; Ganguly, S. Formation of mechanical property gradient along the sheet thickness due to the patterned Fe/Al IMC layers in the interface in dissimilar FSW of HSLA steel to AA 5083. *Mater. Charact.* **2023**, *203*, 113146. [[CrossRef](#)]
50. Yang, Y.; Luo, Z.; Zhang, Y.; Su, J. Dissimilar welding of aluminium to steel: A review. *J. Manuf. Process.* **2024**, *110*, 376–397. [[CrossRef](#)]
51. Chatelier, C.; Anand, K.; Gille, P.; De Weerd, M.C.; Ledieu, J.; Fournée, V.; Resta, A.; Vlad, A.; Garreau, Y.; Coati, A.; et al. Revealing the epitaxial interface between $\text{Al}_{13}\text{Fe}_4$ and Al_5Fe_2 enabling atomic Al interdiffusion. *ACS Appl. Mater. Interfaces* **2023**, *15*, 19593–19603. [[CrossRef](#)] [[PubMed](#)]
52. Liu, Y.; Fan, C.; Wen, B.; Xu, Z.; Fu, R.; Zhang, L. Orientation Relationship of Intergrowth Al_2Fe and Al_5Fe_2 Intermetallics Determined by Single-Crystal X-ray Diffraction. *Metals* **2024**, *14*, 337. [[CrossRef](#)]
53. Bruker AXS Inc. APEX3, SAINT and SADABS. In *Software for Data Reduction, Absorption Correction and Structure Solution*; Bruker AXS Inc.: Madison, WI, USA, 2015.
54. Krause, L.; Herbst-Irmer, R.; Sheldrick, G.M.; Stalke, D. Comparison of silver and molybdenum microfocus X-ray sources for single-crystal structure determination. *J. Appl. Crystallogr.* **2015**, *48*, 3–10. [[CrossRef](#)] [[PubMed](#)]
55. Sheldrick, G.M. Crystal structure refinement with SHELXL. *Acta Crystallogr. C Struct. Chem.* **2015**, *71*, 3–8. [[CrossRef](#)] [[PubMed](#)]
56. Sheldrick, G.M. SHELXT—Integrated space-group and crystal-structure determination. *Acta Crystallogr. A* **2015**, *71*, 3–8. [[CrossRef](#)] [[PubMed](#)]
57. Putz, H.; Brandenburg, K. Diamond 4.2. 2—Crystal and Molecular Structure Visualization. *Crystal. Impact. Kreuzherrenstr.* **2017**, *102*, 53227.
58. Blatov, V.A.; Shevchenko, A.P.; Proserpio, D.M. Applied topological analysis of crystal structures with the program package ToposPro. *Cryst. Growth Des.* **2014**, *14*, 3576–3586. [[CrossRef](#)]

-
59. Akhmetshina, T.G.; Blatov, V.A. A fascinating building unit: Mackay cluster in intermetallics. *Struct. Chem.* **2017**, *28*, 133–140. [[CrossRef](#)]
 60. Sugiyama, K.; Obata, T.; Hiraga, K. The crystalline structure of O-AlFePd. *Mater. Trans.* **2012**, *53*, 1357–1362. [[CrossRef](#)]

Disclaimer/Publisher’s Note: The statements, opinions and data contained in all publications are solely those of the individual author(s) and contributor(s) and not of MDPI and/or the editor(s). MDPI and/or the editor(s) disclaim responsibility for any injury to people or property resulting from any ideas, methods, instructions or products referred to in the content.